Sensor and Simulation Notes
Note 486

Effect of Defocusing on the Prompt Response of an IRA: I. Hyperboloidal Reflector

J. Scott Tyo
Electrical and Computer Engineering Department
University of New Mexico
Albuquerque, NM 87131-1356
tyo@eece.unm.edu

Everett G. Farr
Farr Research, Inc.
614 Paseo del Mar NE
Albuquerque, NM 87123
efarr@farr-research.com

Dean Lawry
Air Force Research Lab/DEHP
3550 Aberdeen SE
Kirtland AFB, NM 87117

November 2003

Abstract

The reflector on an impulse radiating antennas (IRAs) is normally designed to be paraboloidal in shape, and are oriented so that the electrical feed point of the TEM feed line coincides with the focal point of the paraboloid. In many practical cases, the feed point and focal points are not exactly aligned, producing some defocus of the reflector. There are two types of defocus that can be analyzed exactly in the geometric optics approximation: converting the paraboloid into either a hyperboloid or a prolate spheroidal (elliptical cross-section) reflector. The paraboloidal reflector converts the spherical wave emanating from the feed point into a plane wave (i.e. a spherical wave focused at ∞). The hyperboloid converts the expanding spherical wave into a second expanding wave which appears to emanate from the second focal point of the hyperboloid (which is behind the reflector); the prolate spheroid converts the expanding spherical wave into a second spherical wave that converges on the second focal point of the spheroid (which is in front of the reflector). The two cases are roughly equivalent to moving the electrical feed closer to the reflector (hyperboloid) or further from the reflector (prolate spheroid). In this paper, we examine the effect of hyperboloidal defocus. Previously [1], we derived the E- and H-plane responses from an in-focus IRA, and demonstrated that these responses are symmetric with respect to the center of the response. The results shown here demonstrate that the defocusing causes these responses to become *asymmetric*. These results explain the responses that have been measured from supposedly in-focus IRAs in the past.

This work was supported by the Air Force Research Lab, Directed Energy Directorate.

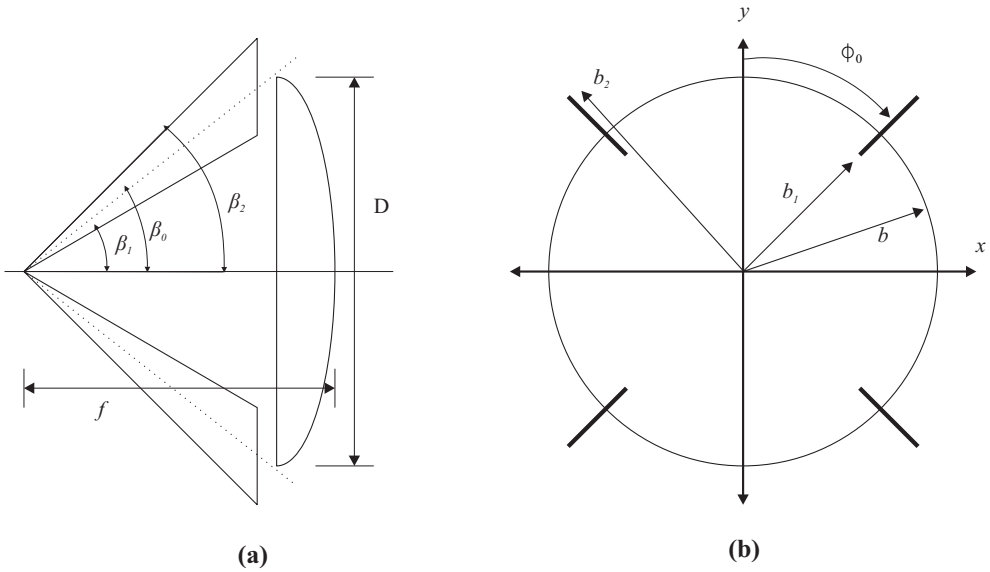

Figure 1: Schematic of a generic 4-arm IRA. The aperture plane is shown here. Various sizes and shapes of apertures can be considered in the physical optics theory.

1 Introduction

The reflectors on an impulse radiating antennas (IRAs) are normally designed to be paraboloidal in shape, and are oriented so that the electrical feed point of the TEM feed line coincides with the focal point of the paraboloid. Geometric optics dictates that such a configuration will convert the spherical wave expanding from the focus into a plane wave in the near field. Physical optics theory can then be employed to predict the prompt radiated field on- and off-boresight from the focused aperture of the IRA [2]. In fact, the solution computed by this method is more accurate than physical optics suggests. For a finite time determined by the size of the aperture and the distance, the geometric optics solution of the aperture fields is exact. Causality dictates that the fields act as if the reflector were infinite until enough time has passed for the edge of the reflector to affect the fields.

We take the aperture A shown in fig. 1 to lie in the $z = 0$ plane and use the source coordinates (x', y') to describe the position in the aperture. Standard aperture theory dictates that we only need to consider the tangential field components on the aperture [3]. Furthermore, the typical feed configurations used in IRAs virtually always have reflection symmetry about the vertical axis [2, 4], allowing us to consider only the principal field component. Without loss of generality, we assume that the principal field component is aligned with the y axis. On-boresight, as well as in the E-plane, the x component of the electric field does not contribute. In the H-plane, theory predicts a contribution from the x-component that is orders of magnitude smaller than the principal component [1]. In practice, the cross polarized radiation is dominated by manufacturing imperfections, especially at the feed point, that are not accounted for in this theory [5].

We take the y-component of the field illuminating the aperture to be

$$E_y(z=0) = E_y(x', y', t). \tag{1}$$

Using physical optics to integrate over the equivalent currents in the aperture plane results in co-polarized radiated fields at distance r far from the aperture in the direction (θ, ϕ) given by [1, 6]

$$E_{co} = \frac{1}{2\pi r c}\left(\hat{\phi}\cos\theta\cos\phi + \hat{\theta}\sin\phi\right)\frac{d}{dt}\iint_A E_y\left(x', y', t' + \frac{\sin\theta\cos\phi x'}{c} + \frac{\sin\theta\sin\phi y'}{c}\right)dx'dy, \tag{2}$$

where $t' = t - r/c$ is the retarded time at the center of the aperture. Eqn. (2) can be used to determine the radiated fields from an aperture A with arbitrary spatiotemporal illumination [1].

IRAs that have parabolic reflectors with coincident electrical feed and optical focal points and excited by a unit step function $u(t)$ have an aperture illumination which is given in the geometric optics approximation as

$$E_{y,ideal}(x', y', t) = E_y(x', y')u(t), \tag{3}$$

in which case (2) predicts that the boresight radiated field is

$$E_{co}(\theta = 0) = \frac{\delta_a(t)V_0 h_a}{2\pi r c f_g}, \tag{4}$$

where

$$h_a = \frac{fg}{V_0}\iint_A E_y(x', y')dx'dy' \tag{5}$$

is the aperture height of the antenna, $f_g = Z_{feed}/\eta_0$ is the geometric impedance factor, and V_0 is the magnitude of the applied step voltage [7]. Off boresight the radiated fields are given as [1]

$$E^h_\phi(r, \theta, t) = \frac{V_0\cot\theta}{2\pi r}\Phi^h\left(-\frac{ct'}{\sin\theta}\right). \tag{6}$$

in the H-plane and

$$E^e_\theta(r, \theta, t) = \frac{V_0}{2\pi r\sin\theta}\Phi^e\left(-\frac{ct'}{\sin\theta}\right). \tag{7}$$

in the E-plane. The quantities Φ^h and Φ^e in (6) and (7) are given as

$$\Phi^h(x) = (1/V_0)\int_{y_{min}}^{y_{max}} E_y(x, y')dy'. \tag{8}$$

and

$$\Phi^e(y) = (1/V_0)\int_{x_{min}}^{x_{max}} E_y(x', y)dx'. \tag{9}$$

[1] This assumes that the spatial symmetry of the illumination meets the conditions discussed above to ignore the cross polarized radiation. If these conditions aren't met, then the integral in (2) must be modified to account for the x-component of the field.

In section 2 we discuss the defocusing of the IRA. In section 3, we present the aperture integration theory for the defocused case. Section 4 contains the discussion of the results and a comparison with experimental data. Section 5 has the conclusions. Appendix A presents the geometry of the hyperboloids considered here.

2 Defocusing the Reflector

In applications where the IRA is to be used to generate large peak fields in a narrow beam centered on boresight, a focused paraboloid is ideal. However, such an antenna is known to have an extremely narrow beam width, especially at high frequencies [1, 8]. Actual IRA measurements indicate 3 dB peak power beam widths on the order of 1° for aperture radii on the order of a few meters [9, 10]. For many applications, including ultra wideband (UWB or hyperband) synthetic aperture radar, such a narrow beam width is undesirable and methods should be taken to broaden the beam. Furthermore, precise collocation of the electrical feed and optical focus is difficult to obtain in practice. The results presented in section 4 below demonstrate that nominally "in focus" IRAs are often slightly *out of focus*.

General considerations for pulse shaping in aperture antennas have been presented previously [11, 12], and Baum has presented a specific strategy for defocusing an IRA by using a deformed hyperboloidal reflector to produce a pulse with desirable spectral content on boresight [13]. Farr, *et al.*, designed and built the multi function IRA which had a mechanism that could move the electrical feed away from the optical focus [14]. In this paper, we examine only the first order perturbations from the paraboloidal reflector. Specifically, we consider a hyperboloidal reflector, which is loosely equivalent to moving the electrical feed closer to a paraboloidal reflector. In a future paper we will examine the use of a prolate spheroidal reflector, which is equivalent to moving the feed away from a paraboloidal reflector[2].

Geometric optics considerations can be used to determine the spatial and temporal variations of the fields that illuminate the aperture as the aperture is assumed to be close to the reflector. Fig. 2 shows the standard ray tracing for the three conic sections mentioned above. We see that a spherical wave that emanates from one focus of the prolate spheroid is converted to a spherical wave that converges on the second focus. As the second focus moves towards $-\infty$, the prolate spheroid approaches a paraboloid, where the second focus is at ∞. Once the second focus starts to move in from $+\infty$, the paraboloid becomes a hyperboloid. Radiation emanating from one focus of the hyperboloid is converted to an expanding spherical wave that appears to emanate from the second focus. In this way, we see that we have three cases: 1) focus in front of the reflector, 2) focus at ∞, 3) virtual focus *behind* the reflector.

In all of the analyses that follow, we will start from a paraboloidal reflector of focal length F and diameter D. We can parameterize the defocus by the angle ϕ_0 shown in fig. 3.

If we take step function excitation of a hyperboloidal reflector as shown in fig. 2, ray

[2]We say loosely equivalent because hyperboloidal and prolate spheroidal reflectors are aberration free, as opposed to the defocused paraboloid.

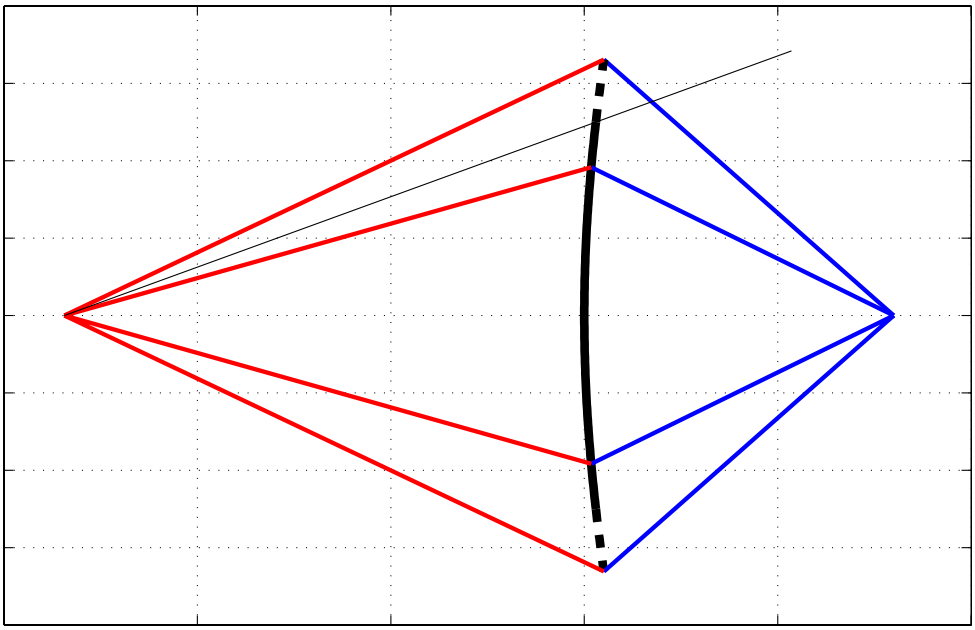

Figure 2: A hyperboloidal reflector converts a spherical wave emanating from one focus of the reflector into a spherical wave that appears to emanate from the second focus. The effect of this is to convert the short TEM feed structure in front of the reflector into an effectively longer TEM horn, at least as far as the prompt response is concerned.

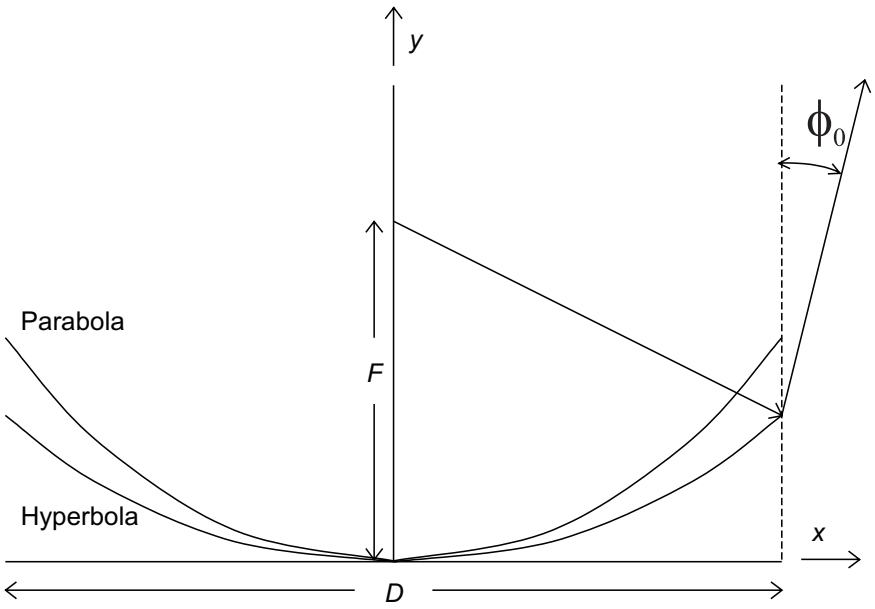

Figure 3: The hyperboloidal reflector is flatter than the corresponding parabolic reflector. The parameter ϕ_0 gives the deviation of the extreme ray in the hyperboloidal case from the direction of focus in the parabolic case.

tracing dictates that we will illuminate an expanding circle in the aperture of radius $\Psi_a(t)$ given as

$$\Psi_a(t) = \sqrt{(2a + ct)^2 - x_0^2}, \tag{10}$$

where a is major axis length of the hyperboloid and x_0 is the distance of the aperture plane from the apex of the reflector. All of the parameters of the hyperboloid are derived in Appendix A. We can modify (1) to

$$E_y(x', y', t) = E_y(x', y')u(\Psi_a(t) - \rho'), \tag{11}$$

where $\rho' = \sqrt{x'^2 + y'^2}$ is the cylindrical radius in the aperture plane. Using (11) in (2) and specializing to the H-plane ($\phi = 0, \pi$) produces

$$E_\phi(r, \theta, \phi; t) = \frac{\cos\theta}{2\pi rc}\frac{d}{dt}\iint_A E_y(x', y')u\left(\Psi_a\left(t' + \frac{\sin\theta x'}{c}\right) - \rho'\right)dx'dy'. \tag{12}$$

Moving the time derivative inside the integral and changing the variables of integration from (x', y') to (ρ', ϕ') produces

$$E_\phi(r, \theta, \phi; t) = \frac{\cos\theta}{2\pi rc}\iint_A E_y(x', y')\delta\left(\Psi_a\left(t' + \frac{\sin\theta x'}{c}\right) - \rho'\right)\frac{\partial\Psi_a\left(t' + \frac{\sin\theta x'}{c}\right)}{\partial t}\rho' d\rho' d\phi'. \tag{13}$$

The integral over the radial coordinate trivially provides

$$E_\phi(r, \theta, \phi; t) = \frac{\cos\theta}{2\pi rc}\oint_C E_y\frac{\partial\Psi_a\left(t' + \frac{\sin\theta x'}{c}\right)}{\partial t}\Psi_a\left(t' + \frac{\sin\theta x'}{c}\right)d\phi', \tag{14}$$

where C is the contour that satisfies

$$\rho' = \Psi_a\left(t' + \frac{\sin\theta x'}{c}\right). \tag{15}$$

Substituting (10) in (15) and carrying through the algebra produces

$$\frac{\left(x' - \frac{\sin\theta}{\cos^2\theta}(ct' + 2a)\right)^2}{\left(\frac{(ct'+2a)^2 - (x_0\cos\theta)^2}{\cos^4\theta}\right)} + \frac{y'^2}{\left(\frac{(ct'+2a)^2 - (x_0\cos\theta)^2}{\cos^2\theta}\right)} = 1. \tag{16}$$

Eqn. (16) is clearly the equation for an ellipse. The center of this ellipse is at

$$h = \frac{\sin\theta}{\cos^2\theta}(ct' + 2a), \tag{17}$$

and the lengths of the major and minor axes of the ellipse are

$$a = \frac{(ct' + 2a)^2 - (x_0\cos\theta)^2}{\cos^4\theta}, \tag{18}$$

$$b = \frac{(ct' + 2a)^2 - (x_0\cos\theta)^2}{\cos^2\theta}, \tag{19}$$

On boresight ($\theta = 0$), this ellipse is centered at the origin, but for off-boresight angles, the center of the ellipse starts at some finite position and moves away from the origin linearly as time progresses. Likewise, the lengths of the major and minor axes increase quadratically with time. On boresight, the ellipse collapses to a circle as $a = b$ in (16). As the off-boresight angle θ increases, the ellipse becomes more and more eccentric.

Table 1: Parameters of IRAs discussed in this paper. The aperture configurations are S: standard (focused circle of symmetry), NF: non-floppy (focused circle corresponding to the outer edge of the feed arms), NFE: non-floppy with exclusion (same as NF with trimming). All antennas analyzed here assume that the radius of the focused aperture is 1 m.

Z_{feed} [Ω]	# of arms	feed angle [$^\circ$]	aperture
400	2	90	S
400	2	90	NF
200	4	60	S
200	4	60	NFE

3 Aperture Plane Contours and Step Responses

In this section, we will demonstrate the effects of (16) – (19) in predicting the radiated step response from IRAs. The cases analyzed here are for the development of the compact IRA, and the parameters are given in table 1. The first configuration is a 400 Ω, two-arm configuration corresponding to one polarization in the dual polarization IRA [15]. The second configuration is a 200Ω, 4-arm feed structure with the non-floppy configuration that is necessary when the reflector is not self supporting [1]. The S (standard) aperture is when the entire circle of symmetry of the IRA is focused. The NF (non-floppy) configuration is when the entire circle inside the feed arms is focused. The NFE configuration is the same size as the NF configuration, but the destructively contributing portions of the aperture are eliminated by trimming [16, 17]. Examples of these apertures are shown in fig. 4.

3.1 H-Plane Responses

Fig. 5, fig. 7, and fig. 9 show the progression of the contour C in (14) when the defocus parameter is $\phi_0 = 0.01^\circ$ (approximately in focus) , 5°, and 10°, respectively. The curves are plotted for $\theta = 0^\circ$, 2.5°, and 5° in the H-plane. The specific configuration corresponding to these figures is the 400 Ω, 2-arm IRA with the standard (S) aperture configuration. The contours traced out for the other cases are identical, only the aperture fields are slightly changed. Fig. 6, fig. 8, and fig. 10 show the radiated signal in response to a 25-ps-rise time step for each of these cases. The vertical axis units are arbitrary, but correspond to [V/m], and all three figures are presented with the same arbitrary units.

Analysis of fig. 5 - fig. 10 provide insight about how defocusing alters the radiated step response. For the nearly in-focus case (fig. 5 and fig. 6), the expanding circle on boresight rapidly fills up the aperture. The ideal step response is less than 4 ps in duration (data not shown), and the corresponding boresight response to the 25-ps-rise step is almost exactly equal to the derivative of the applied voltage waveform [18]. As the observation direction moves off boresight, the center of the expanding ellipse given by (17) is far from the origin. The portion of the ellipse that intersects the focused aperture is approximately a straight line, making the step response proportional to $\Phi^{(h)}$ and $\Phi^{(e)}$ in (8) and (9).

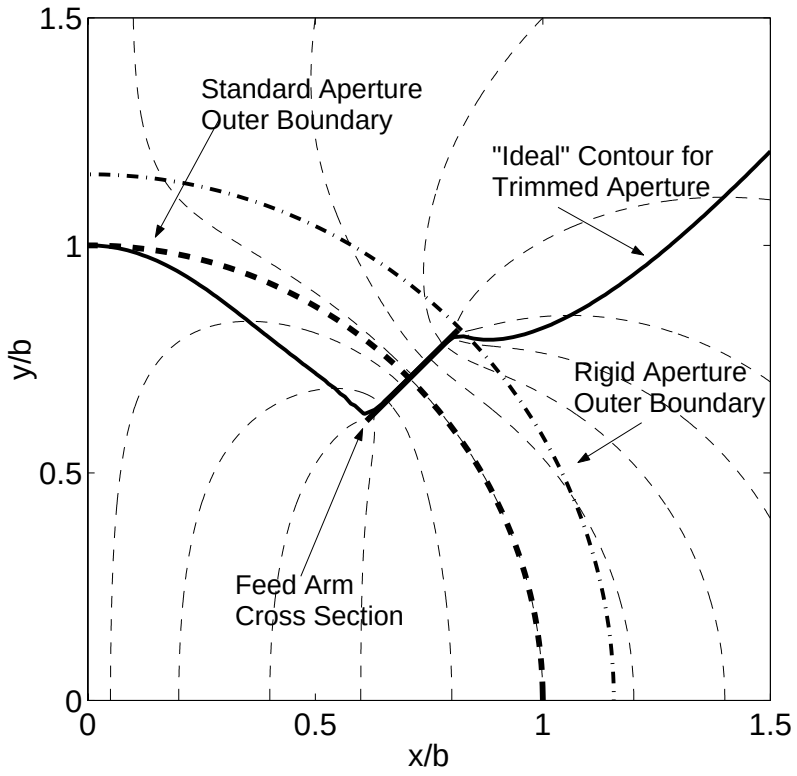

Figure 4: Three aperture configurations considered in this study. The outer boundary is the same for the NF and NFE configurations, but the portions of the NFE aperture above the "ideal contour" are trimmed away.

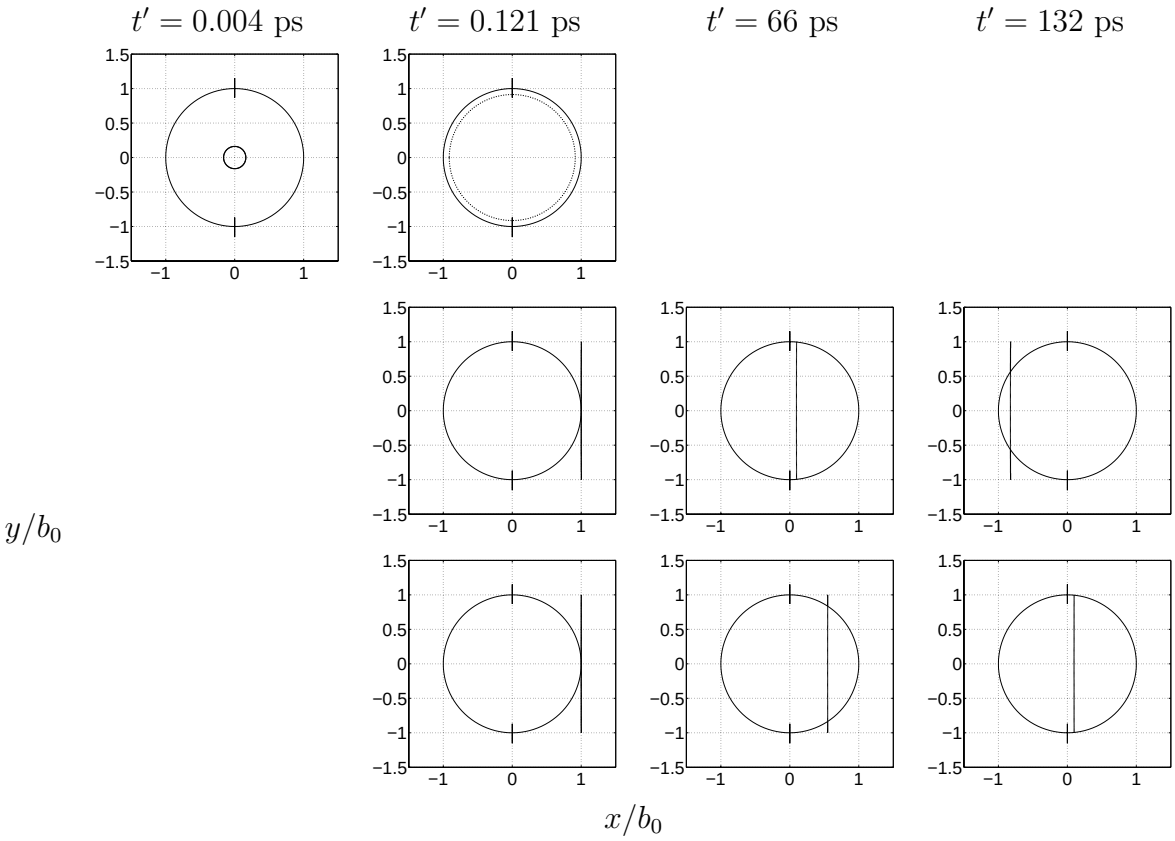

Figure 5: Snapshots of the contour of integration for three viewing angles for an in-focus IRA (ϕ_0 =0.01°). The three rows (from top to bottom) are at $\theta = 0°$, 2.5°, and 5°. The configuration analyzed here has the NF aperture and 400 Ω, 2-arm feed.

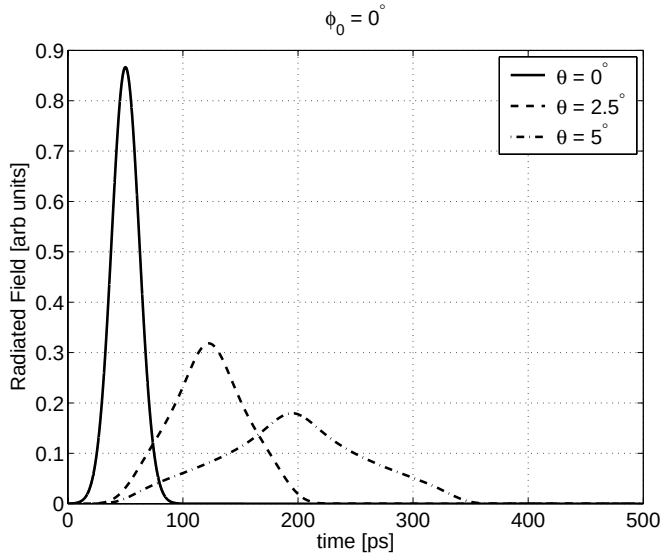

Figure 6: Radiated step response to a 25-ps-rise time step for cases in fig. 5.

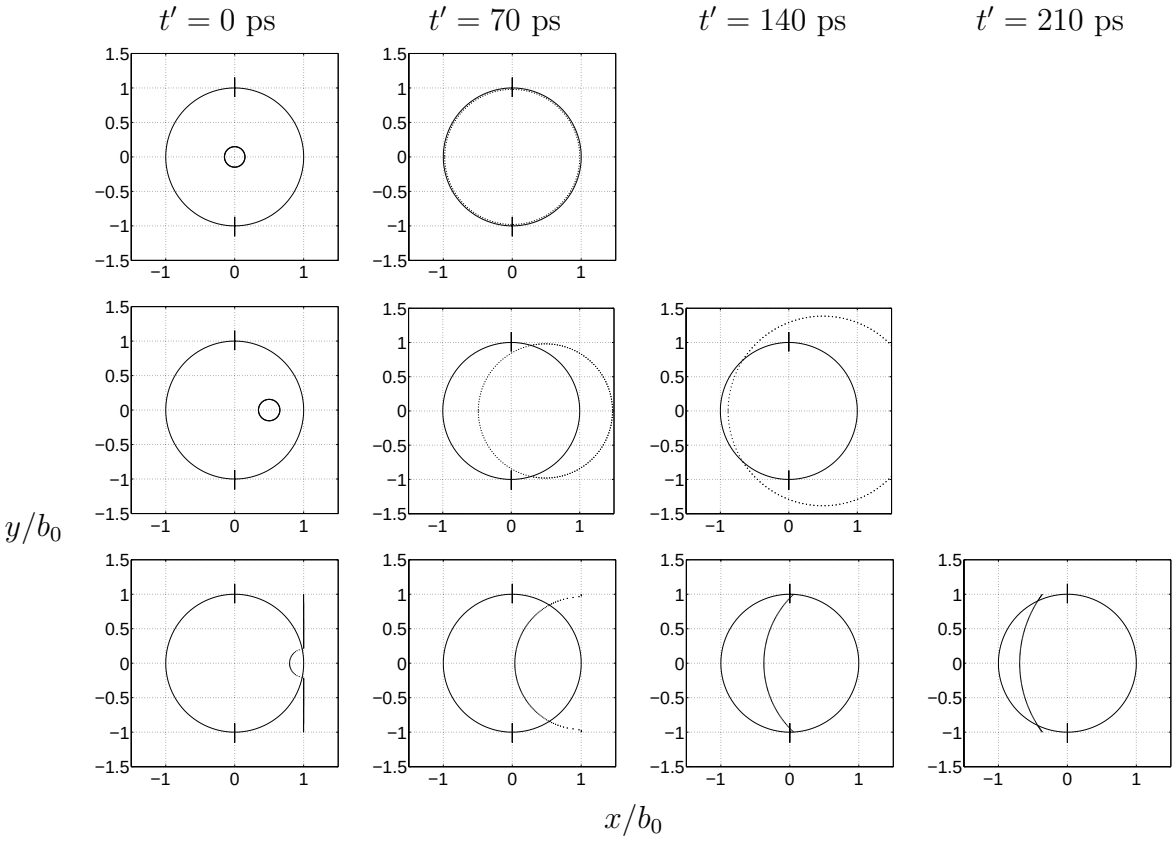

Figure 7: Snapshots of the contour of integration for three viewing angles for an IRA with ϕ_0 =5°. The three rows (from top to bottom) are at $\theta = 0°$, 2.5°, and 5°. The configuration analyzed here has the NF aperture and 400 Ω, 2-arm feed.

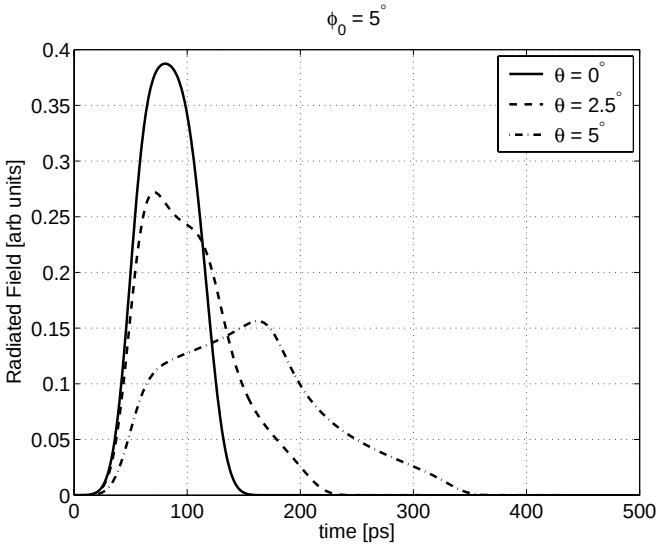

Figure 8: Radiated step response to a 25-ps-rise time step for cases in fig. 7.

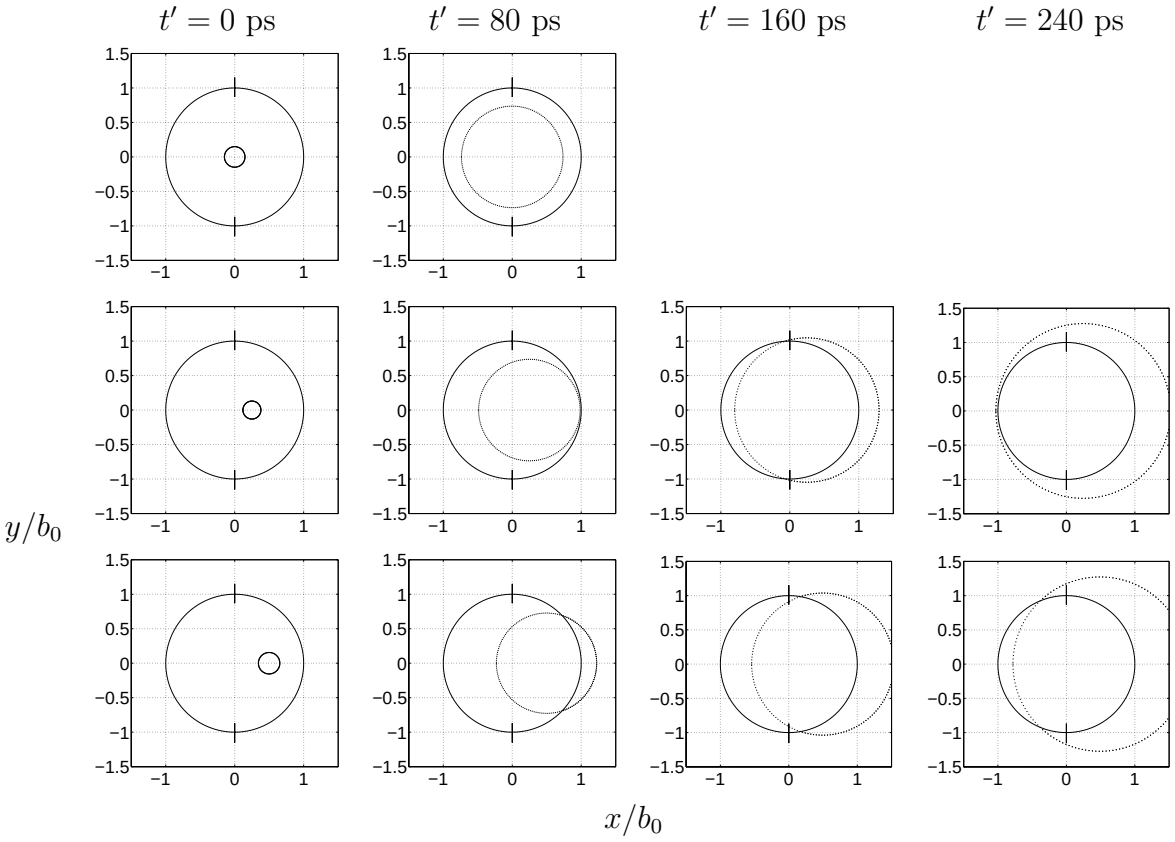

Figure 9: Snapshots of the contour of integration for three viewing angles for an IRA with ϕ_0 =10°. The three rows (from top to bottom) are at θ = 0°, 2.5°, and 5°. The configuration analyzed here has the NF aperture and 400 Ω, 2-arm feed.

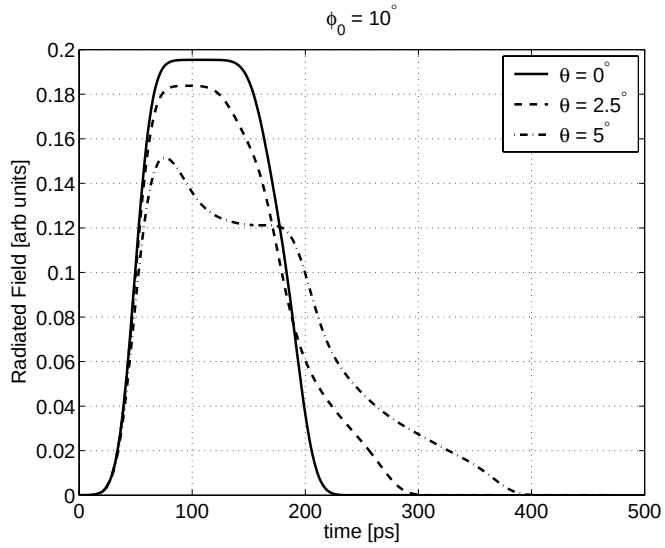

Figure 10: Radiated step response to a 25-ps-rise time step for cases in fig. 9.

For the out of focus cases, the boresight response is governed by an expanding circle that covers the aperture much more slowly than for the focused IRA. The radiated responses to the 25-ps-rise time steps in fig. 8 and fig. 10 are much lower in amplitude and much larger in width (which is necessary to keep the integrated area constant, as predicted by Baum [7]. As the observation direction moves off boresight, the center of the expanding ellipse is much closer to the origin than is the case for the in-focus IRA. The contour C therefore has much more curvature, giving rise to step responses that are asymmetric in time. $\Phi^{(h)}$ and $\Phi^{(e)}$ are symmetric, as are the responses shown in fig. 6. Similar step response data (presented on the same vertical scales) for the other configurations in table 1 are presented in fig. 11 - fig. 13. A detailed analysis of amplitudes, pulse widths, and gain in the frequency domain are presented in section 4.

3.2 E-Plane

The behavior of this system in the E-plane is qualitatively similar to that in the H-plane. Namely the roles of x and y are reversed in (16) – (19). The contour C in (14) is once again an ellipse that expands, but it is centered on the y-axis instead of the x-axis. The expanding contour for the case of the 200 Ω IRA with 4 feed arms at 60° and the NF aperture configuration is shown in fig. 14. The radiated step response for this case is shown in fig. 15. The step responses for all other configurations are shown in fig. 16 – fig. 18.

One of the most important features to note about the E-plane response as compared with the H-plane response is that the response can actually become negative without trimming. Referring to fig. 14, note that as the integration contour C sweeps across the aperture from the top, it first overlaps with regions that are dominated by an E_y that contributes destructively to the integral in (5). We see this manifested in several of the untrimmed E-plane responses in fig. 16 – fig. 18. However, once the destructively contributing portions of the aperture have been trimmed [16, 17], the responses are once again completely positive, as expected [1].

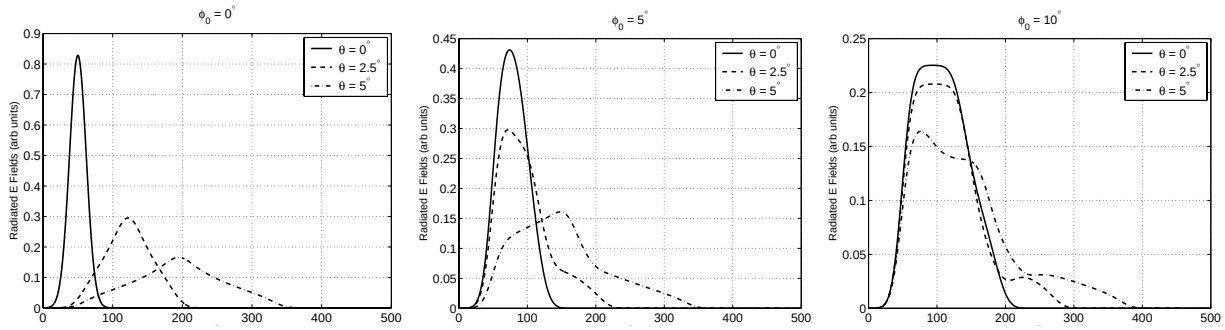

Figure 11: Responses to the 25-ps-rise time step for $Z = 400\ \Omega$ with the NF configuration and 2 feed arms.

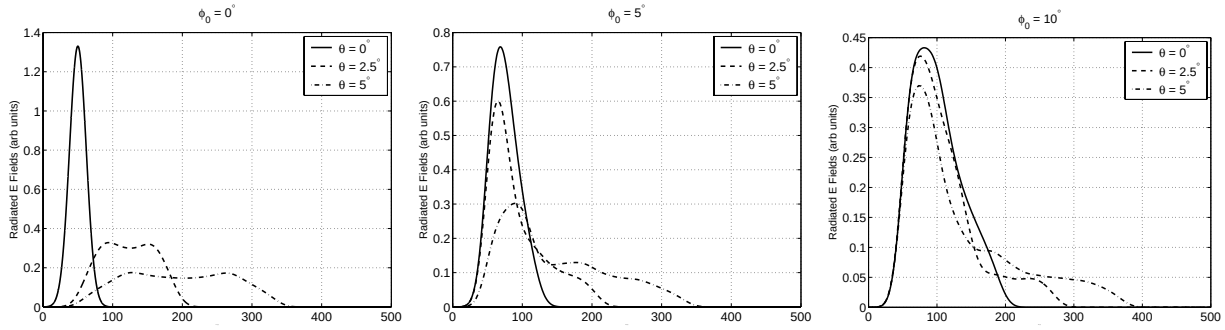

Figure 12: Responses to the 25-ps-rise time step for $Z = 200\ \Omega$ with the NF configuration and 4 feed arms.

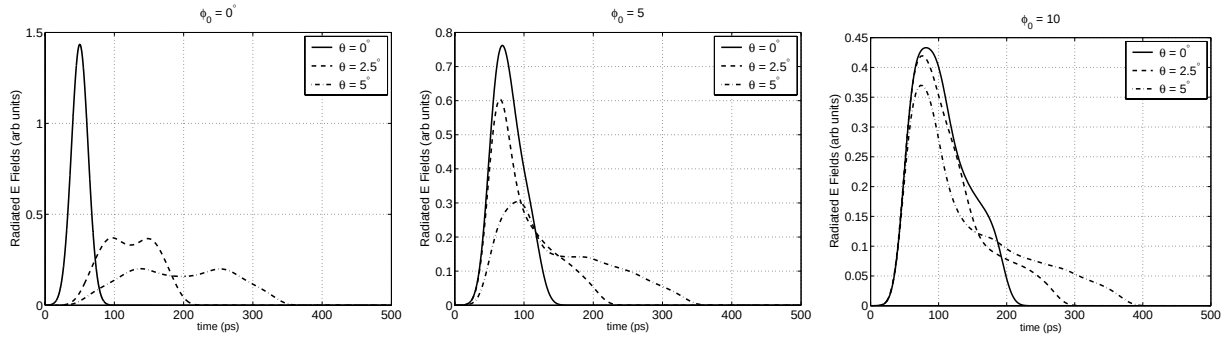

Figure 13: Responses to the 25-ps-rise time step for $Z = 200\ \Omega$ with the NFE configuration and 4 feed arms.

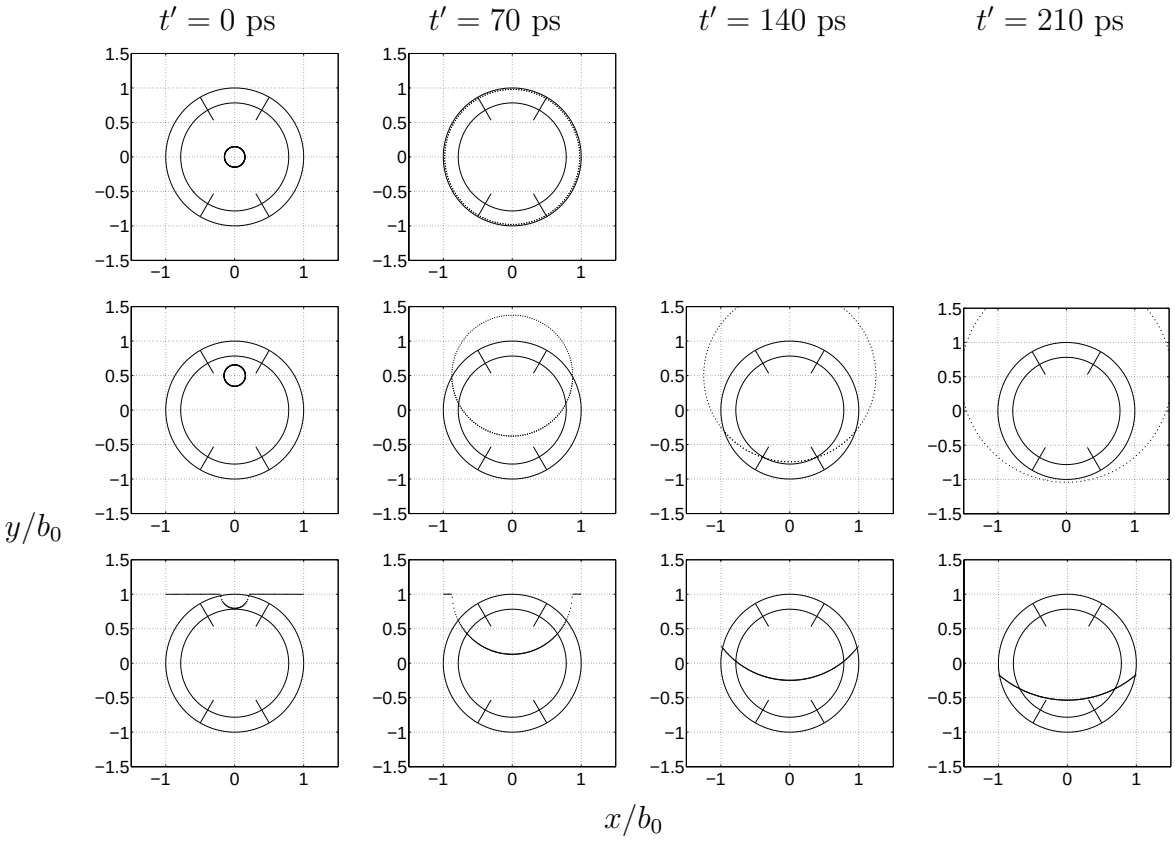

Figure 14: Snapshots of the contour of integration for three viewing angles for an IRA with ϕ_0 =5°. The three rows (from top to bottom) are at $\theta = 0°$, 2.5°, and 5° in the E-plane. The configuration analyzed here has the NF aperture and 200 Ω, 4-arm feed.

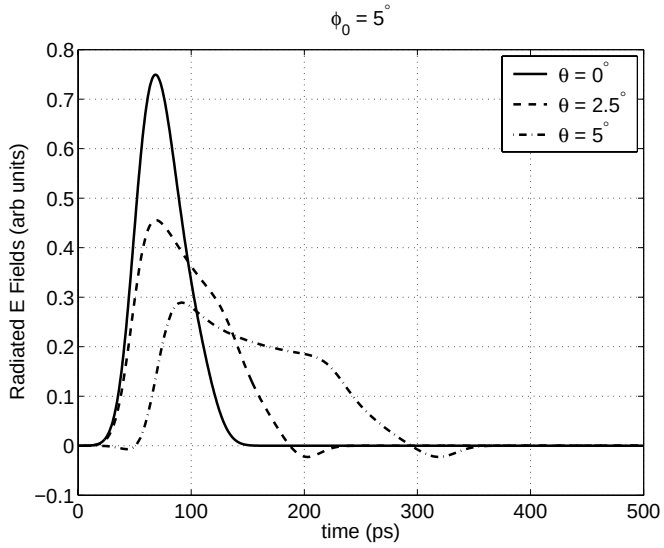

Figure 15: Radiated step response to a 25-ps-rise time step for cases in fig. 14.

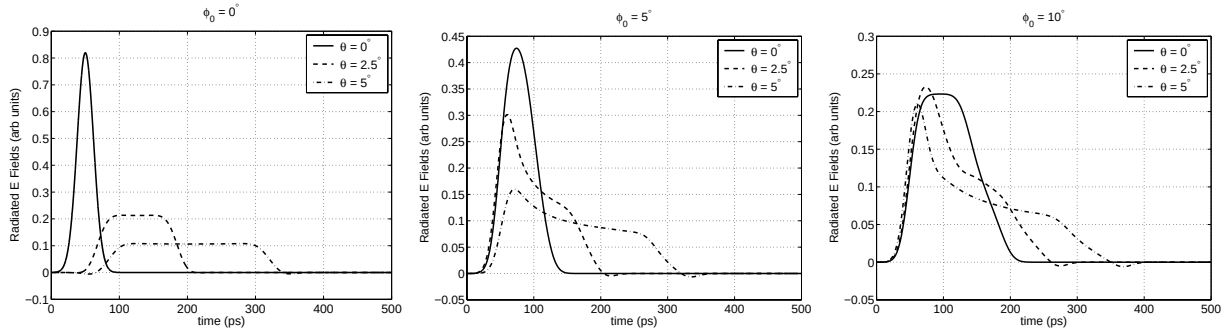

Figure 16: Responses to the 25-ps-rise time step for $Z = 200\ \Omega$ with the NF configuration and 4 feed arms. Responses are for angles in the E-plane

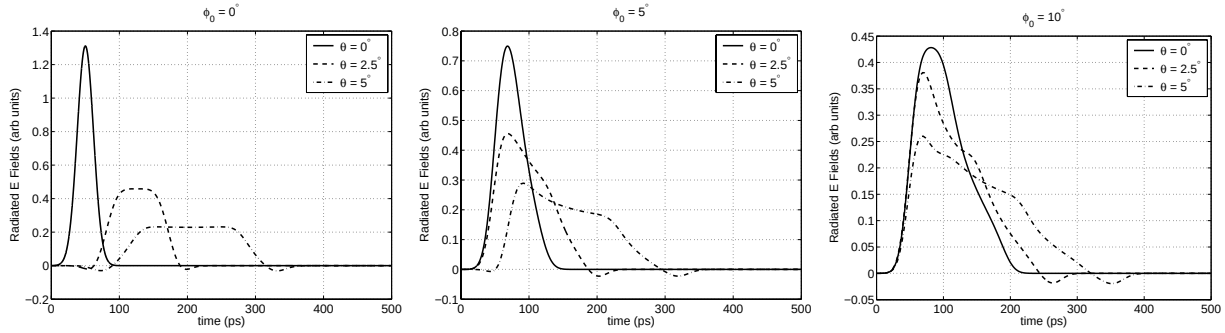

Figure 17: Responses to the 25-ps-rise time step for $Z = 200\ \Omega$ with the NF configuration and 4 feed arms. Responses are for angles in the E-plane

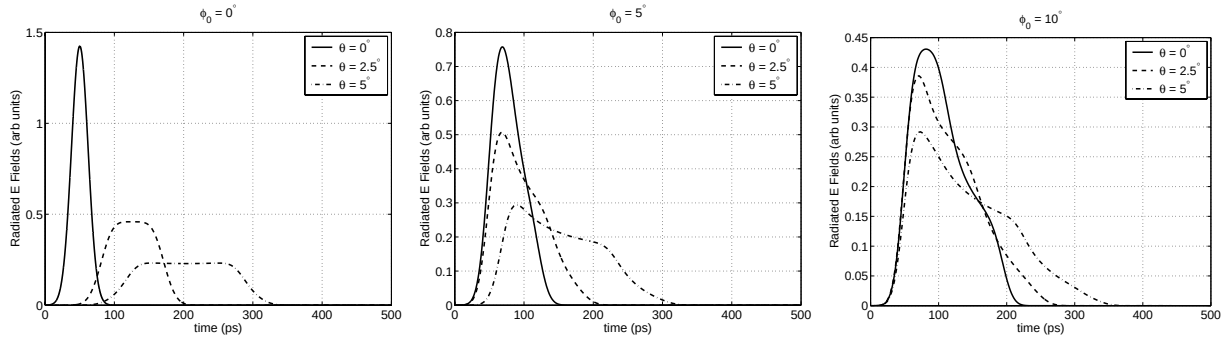

Figure 18: Responses to the 25-ps-rise time step for $Z = 200\ \Omega$ with the NFE configuration and 4 feed arms. Responses are for angles in the E-plane

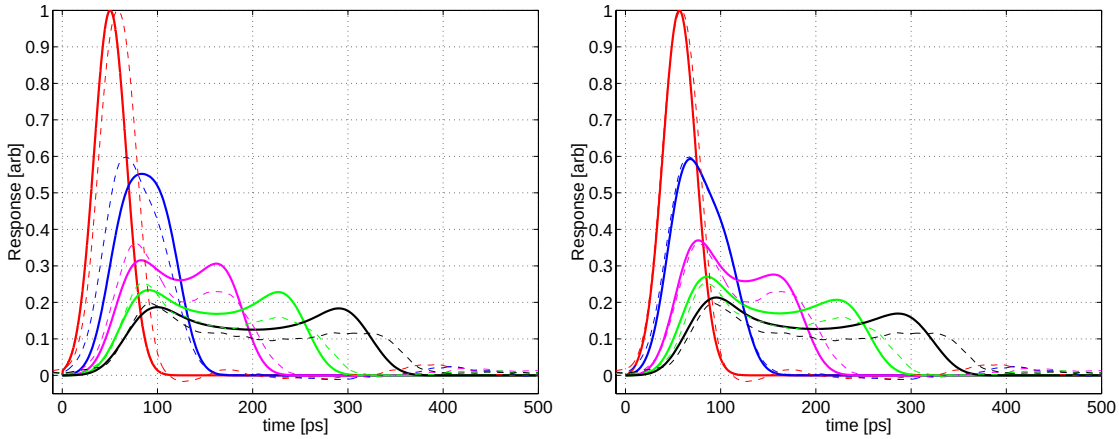

Figure 19: H-plane responses predicted for a 1-m diameter half IRA with $\phi_0 = 0°$ (left) and $\phi_0 = 1.6°$ (right) compared with measurements. The solid curve represents the theoretical predictions and the points are from the measured response of a nominally in focus 1-m-diameter half IRA. The curves are at $\theta = 0°$, 1.25°, 2.5°, 3.75°, 5°.

4 Discussion

4.1 Comparison With Experimental Data

As yet, we have not completed any new experiments with precisely controlled defocus as described here. However, the results presented above can be used to analyze radiation patterns measured from IRAs in order to determine how far out of focus they might be. In an earlier paper [1], we presented a comparison between theoretical predictions and experimental measurements of off boresight radiation from a nominally focused IRA. Fig. 19 shows a comparison of the measured H-plane responses from a nominally in focus, 1-m-diameter, Half IRA compared with the in focus responses predicted by responses predicted for an IRA with $\phi_0 = 0°$ and $\phi_0 = 1°$ (6). The details of this physical antenna that was measured and the experimental configuration are described elsewhere [10]. The theory assumes a Gaussian-rise step with $\sigma = 17$ ps. The slightly out-of-focus theory does a better job of predicting the radiated response. With $\phi_0 = 1°$ the magnitude of the first peak and the rising portion of the waveform are extremely accurately reproduced. The magnitude of the second peak is overpredicted by the theory, but the defocused theory matches the experiment more faithfully.

Fig. 20 shows similar response curves for the E-plane. The E-plane predictions are remarkably accurate. Note that the amount of defocus that fits the data in the E-plane and the H-plane are different. This is plausible, since the half IRA was formed by physically cutting a paraboloidal reflector in half, which could lead to different distortions in the two planes. However, no attempt has been made to characterize the curvature of this antenna.

The modification of the theory discussed in this paper capture many of the salient features of the experimentally measured response. First and most importantly, the asymmetric response in the H-plane is predicted. In addition, the theory predicts the faster rise

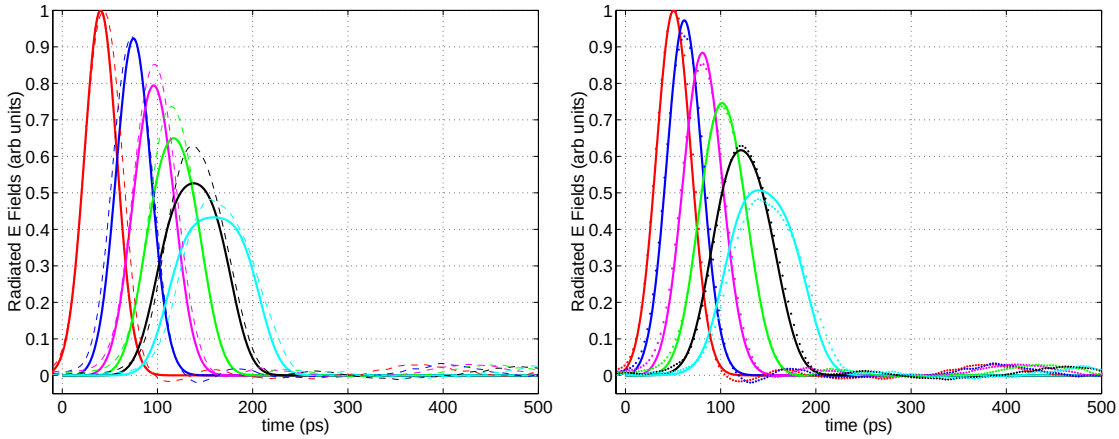

Figure 20: E-plane responses predicted for a 1-m diameter half IRA with $\phi_0 = 0°$ (left) and $\phi_0 = 1.6°$ (right) compared with measurements. The solid curve represents the theoretical predictions and the points are from the measured response of a nominally in focus 1-m-diameter half IRA. The curves are at $\theta = 0°$, $1.2°$, $2.2°$, $3.2°$, $4.2°$, and $5.2°$.

time and slower fall time that is measured off boresight than is predicted by (6) and (7). Based on this comparison, we can draw the conclusion that the nominally in focus half IRA is as much as 1° out of focus. It is this defocus that provides the final upper limit to the high frequency performance of the IRA.

4.2 Defocused IRA Gain

When the IRA is to be used as a broadband antenna, then frequency domain parameters such as gain are important to consider. Fig. 21 presents the absolute gain of a nominally in focus IRA with completely perfect construction in the H- and E-planes. The IRA considered here is the 200 Ω IRA with four feed arms and the NFE aperture. The colormap used is that proposed by Rappaport, *et al.*. [19]. Fig. 22 presents the same data, only normalized so that the gain on boresight is constant as a function of frequency. This is equivalent to looking at the step transmit response in the frequency domain. The data in fig. 21 and fig. 22 are clearly unrealistic. The perfect focus and construction predict that the gain will increase on boresight like f^2. In reality, manufacturing imperfections, including defocus, limit this performance. As the gain increases, the beam width correspondingly decreases, giving rise to a beam width that is often less than 1° wide [1, 5].

In contrast, fig. 23 presents the absolute gain for the same IRA that is now assumed to have a hyperboloidal defocus with $\phi_0 = 5°$. Fig. 25 shows the normalized gain. Fig. 24 presents the absolute gain for the same IRA that is now assumed to have a hyperboloidal defocus with $\phi_0 = 10°$. For the defocused IRA, we see several things. First, there is an expected reduction in absolute boresight gain at high frequencies. The gain at low frequencies is unmodified. The decreased gain on boresight also gives rise to a broadening of the antenna beam width. In fact, this antenna appears to be approximately constant

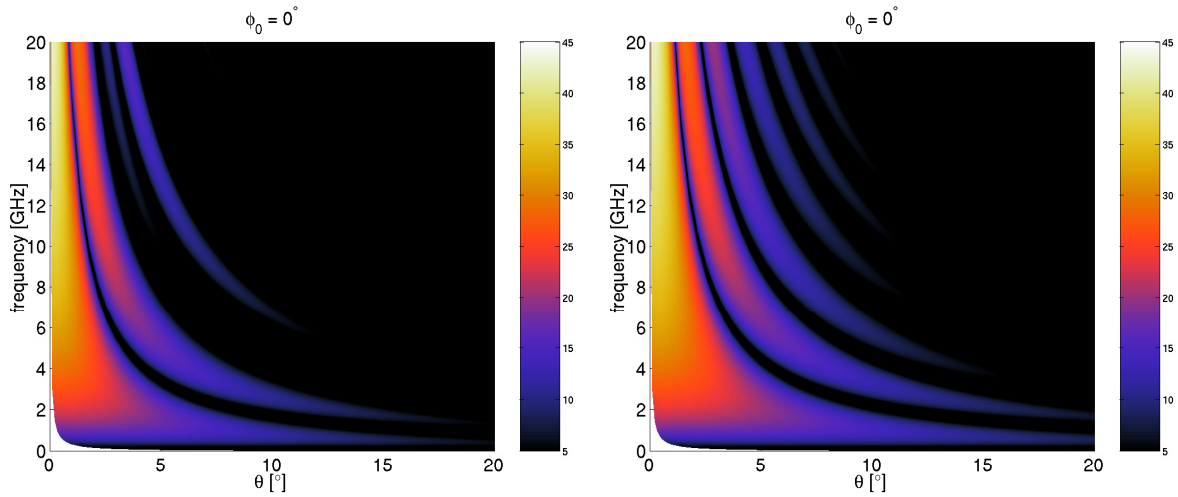

Figure 21: Absolute gain of an ideal IRA. This IRA has no defocus, and no low-frequency cutoff. The left panel is the H-plane, the right panel is the E-plane.

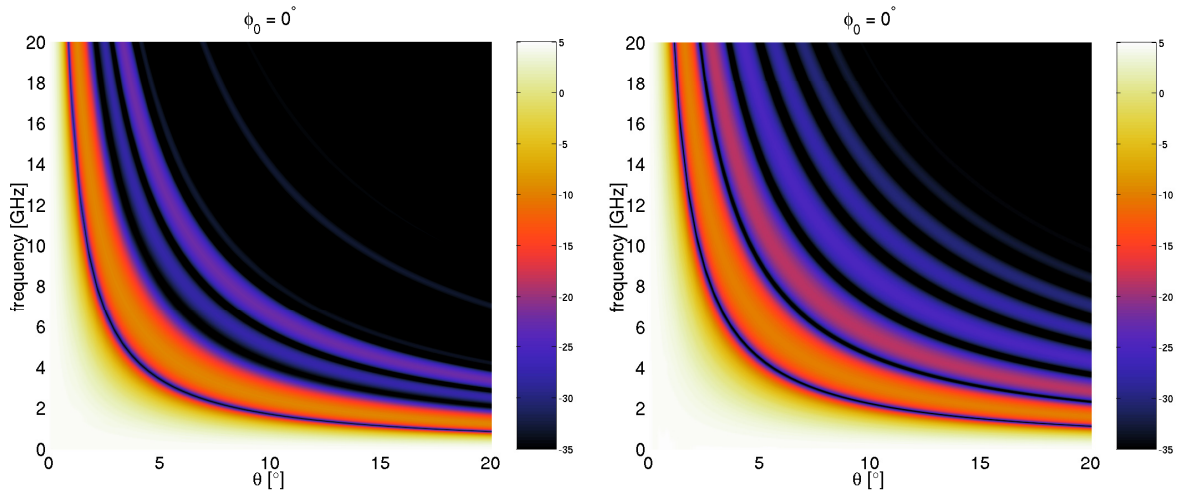

Figure 22: Normalized gain of an ideal IRA. This IRA has no defocus, and no low-frequency cutoff. The left panel is the H-plane, the right panel is the E-plane.

beam width over a large range of frequencies. Such performance should be expected, as the hyperboloidal reflector converts the short TEM feed structure in fig. 1 into the effectively longer image TEM structure as depicted in fig. 2. TEM horns have gain that increases like f^2 at low frequencies before rolling over and appearing as constant gain over a fairly broad frequency range [20]. In addition, it is well known that the beam width from a TEM horn is closely related to the flare angle, especially in the E-plane.

Fig. 26 shows the normalized gain.

5 Conclusions

In this paper, we have developed the theory for radiation from defocused IRAs. The theory is based on a general time domain physical optics formalism that has been simplified to deal with the specific case of an IRA fed by a balanced, TEM feed structure. Radiation from general aperture illuminations that are not solutions to the TEM mode are also possible, but require moving back to the full physical optics formalism.

The theory as developed in this paper provides a basis for the previously unexplained off-boresight responses recorded from fabricated IRAs. Previously it was conjectured that the asymmetric H-plane response as presented in fig. 19 might be due to aperture blockage or other effects. The current theory seems to explain the experimental results, especially in the E-plane. In the H-plane, the agreement is not quite as good. It was found that allowing $\phi_0 = 1^\circ$ does an excellent job of matching the first peak amplitude and the risetime, but misses the second peak. Allowing for more defocus does a better job of predicting the relative amplitudes of the first and second peaks, but overpredicts the amplitude of the response off boresight. Some poten

The current paper considers only the case of aberration-free, hyperboloidal reflectors. In real systems, the defocus could be due to deviations of the parabolic reflector from the specified shape, or it could be due to a misalignment between the electric and optical feed of the IRA. Both of these cases would create defocus with aberrations, and those aberrations might have an effect on the off-boresight fields (or more specifically, the off axis fields). In a future paper we will consider the effects of elliptical defocus, which causes the IRA to be focused at a specific location in front of the reflector. It remains to be seen what the effects of this type of defocus are for the far radiated fields.

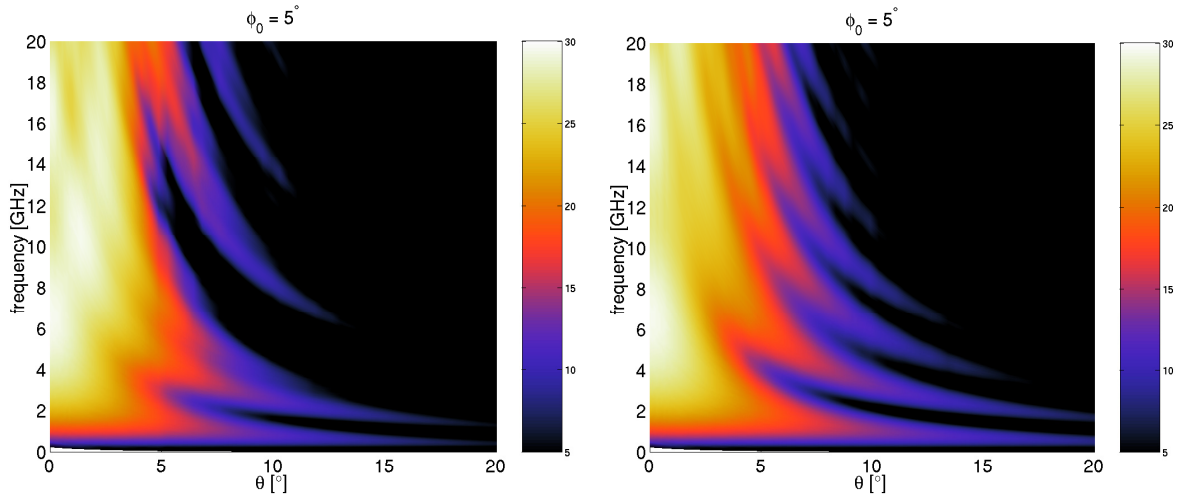

Figure 23: Absolute gain of defocused IRA with $\phi_0 = 5°$. The analysis of this antenna does not include the low frequency cutoff. The left panel is the H-plane, the right panel is the E-plane.

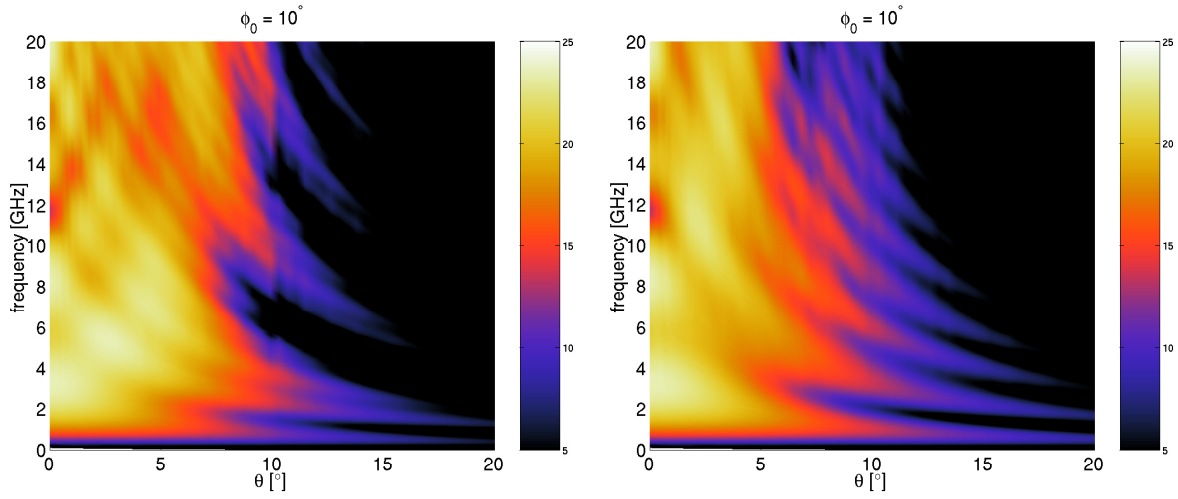

Figure 24: Absolute gain of defocused IRA with $\phi_0 = 10°$. The analysis of this antenna does not include the low frequency cutoff. The left panel is the H-plane, the right panel is the E-plane.

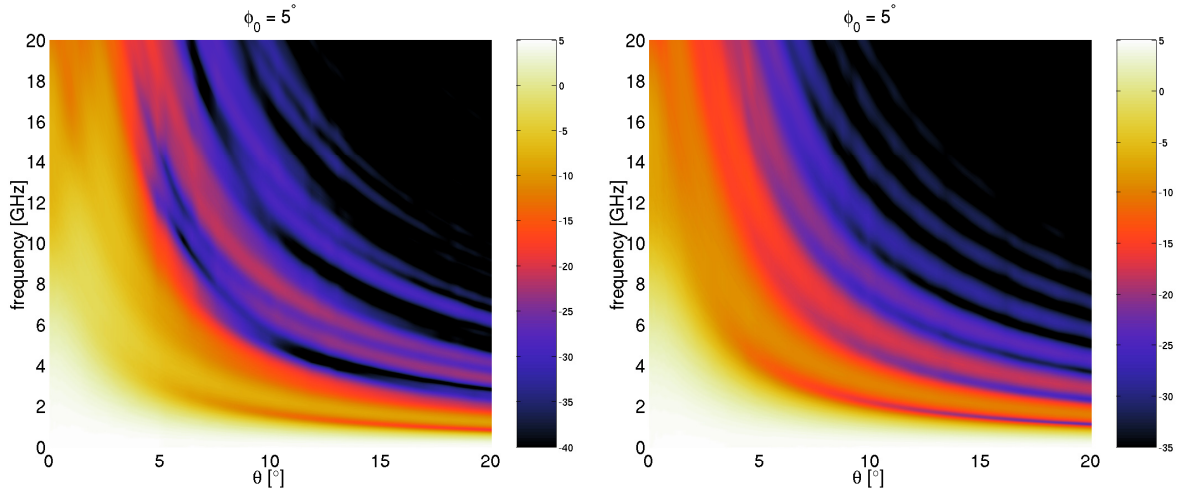

Figure 25: Normalized gain of defocused IRA with $\phi_0 = 5°$. The analysis of this antenna does not include the low frequency cutoff. The left panel is the H-plane, the right panel is the E-plane.

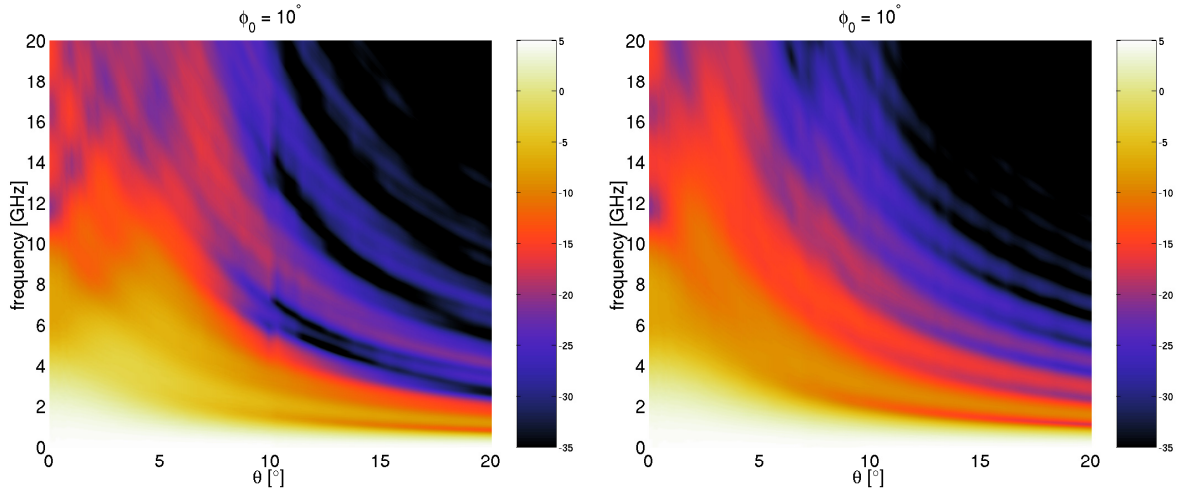

Figure 26: Normalized gain of defocused IRA with $\phi_0 = 10°$. The analysis of this antenna does not include the low frequency cutoff. The left panel is the H-plane, the right panel is the E-plane.

A Hyperbola

In this appendix, we present the algebraic derivations of the parameters of the hyperboloidal reflector that is deviated from a paraboloidal reflector by the parameter ϕ_0 as depicted in fig. 3.

The parabola that gives the reflector is given by the equation

$$y = \frac{1}{4F}x^2. \tag{20}$$

The hyperbola is given by the general expression

$$\left(\frac{y-k}{a}\right)^2 - \left(\frac{x-h}{b}\right)^2 = 1. \tag{21}$$

In our case, we will take the apex of one of the hyperboloidal sheets to be at the origin yielding

$$\begin{aligned} k &= -a \\ h &= 0. \end{aligned} \tag{22}$$

We choose the parameters such that the distance c from the center of the hyperbola to one of the focal points is

$$c = a + F, \tag{23}$$

which makes the distance from the apex of the two reflectors to their respective focal points the same. The general relationships between a, b, and c yield

$$a^2 + b^2 = c^2 \tag{24}$$

$$b^2 = c^2 - a^2 \tag{25}$$

$$b^2 = F(2a + F) \tag{26}$$

From fig. 27 we see that

$$\tan\phi_0 = \frac{(D/2)}{y_0 + a + c} \tag{27}$$

At the edge of the reflector $x_0 = D/2$ and we have

$$y_0 + a = a\sqrt{1 + \frac{(D/2)^2}{F(2a+F)}}. \tag{28}$$

Combining (27) and (28) we find that

$$q = \frac{D/2}{a\sqrt{1 + \frac{(D/2)^2}{F(2a+F)}} + a + F}, \tag{29}$$

where $q = \tan\phi_0$. If we define the parameter $w = D/2 - qF$ we can write the following quadratic equation to compute the length of the major axis a of the hyperbola:

$$\left(\left(\frac{qD}{2}\right)^2 + 4Fqw\right)a^2 + (2qwF^2 - 2Fw^2)a - F^2w^2 = 0. \tag{30}$$

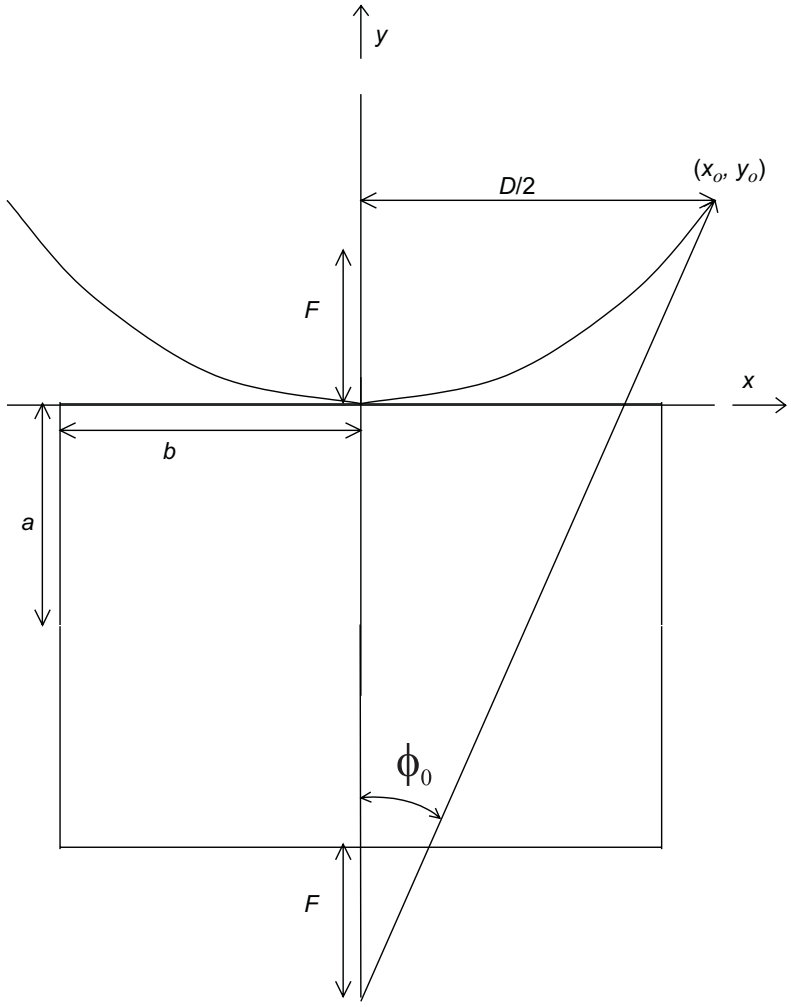

Figure 27: Geometry of the hyperbola that gives the shape of the defocused reflector.

References

[1] J. S. Tyo, E. G. Farr, L. H. Bowen, and L. Altgilbers, "IRA variations useful for flexible feed arm," in *Sensor and Simulation Notes #472* (C. E. Baum, ed.), Albuquerque, NM: Air Force Research Laboratory, 2002. contact AFRL Public Affairs +1-505-846-1911.

[2] C. E. Baum, E. G. Farr, and D. V. Giri, "Review of impulse-radiating antennas," in *Review of Radio Science* (W. R. Stone, ed.), pp. 403–439, New York: Oxford U. Press, 1999.

[3] C. A. Balanis, *Advanced engineering electromagnetics*. New York: Wiley, 1989.

[4] E. G. Farr, C. E. Baum, and C. J. Buchenauer, "Impulse radiating antennas II," in *Ultra-Wideband, Short-Pulse Electromagnetics 2* (L. Carin and L. B. Felson, eds.), pp. 159–170, New York: Plenum Press, 1995.

[5] L. H. Bowen, E. G. Farr, C. E. Baum, T. C. Tran, and W. D. Prather, "Experimental results of optimizing the location of feed arms in a collapsible IRA and a solid IRA," in *Sensor and Simulation Notes #450* (C. E. Baum, ed.), Albuquerque, NM: Air Force Research Laboratory, 2000.

[6] E. G. Farr and C. E. Baum, "Radiation pattern of reflector impulse radiating antennas: early time response," in *Sensor and Simulation Notes #358* (C. E. Baum, ed.), Albuquerque, NM: Phillips Laboratory, 1993. contact AFRL Public Affairs +1-505-846-1911.

[7] C. E. Baum, "Aperture efficiencies of IRAs," in *Sensor and Simulation Notes #328* (C. E. Baum, ed.), Albuquerque, NM: Phillips Laboratory, 1991. contact AFRL Public Affairs +1-505-846-1911.

[8] D. V. Giri and C. E. Baum, "Temporal and spectral radiation on boreight of a reflector type of impulse radiating antenna (IRA)," in *Ultra-Wideband, Short-Pulse Electromagnetics 3* (C. E. Baum, L. Carin, and A. P. Stone, eds.), pp. 65–72, New York: Plenum, 1997.

[9] D. V. Giri, H. Lackner, I. D. Smith, D. W. Morton, C. E. Baum, J. R. Marek, W. D. Prather, and D. W. Scholfield, "Design, fabrication, and testing of a paraboloidal reflector antenna and pulser system for impulse-like waveforms," *IEEE Trans. Plasma Sci.*, vol. 25, pp. 318–326, 1997.

[10] J. S. T. S. H. Schoenberg, "Radiated field measurements from a 1-m-diameter half IRA," in *Sensor and Simulation Notes #471* (C. E. Baum, ed.), Albuquerque, NM: Air Force Research Laboratory, 1999. contact AFRL Public Affairs +1-505-846-1911.

[11] E. Heyman and T. Melamed, "Certain considerations in aperture synthesis of ultrawideband/short-pulse radiation," *IEEE Trans. Antennas Propagat.*, vol. 42, pp. 518 – 525, 1994.

[12] R. W. Ziolkowski, "Properties of electromagnetic beams generated by ultra-wide bandwidth pulse-driven arrays," *IEEE Trans. Antennas Propagat.*, vol. 40, pp. 888 – 905, 1992. and comment and reply in T-AP, **41**:520-522 (1993).

[13] C. E. Baum, "Antenna aperture synthesis for hyperband SAR measurements," in *Sensor and Simulation Notes #66* (C. E. Baum, ed.), Albuquerque, NM: Air Force Research Laboratory, 2002. contact AFRL Public Affairs +1-505-846-1911.

[14] E. G. Farr, C. E. Baum, and W. D. Prather, "Multifunciton impulse radiating antennas: theory and experiment," in *Sensor and Simulation Notes #413* (C. E. Baum, ed.), Albuquerque, NM: Air Force Research Laboratory, 1997. contact AFRL Public Affairs +1-505-846-1911.

[15] E. G. Farr, L. H. Bowen, and D. I. Lawry, "A dual polarity impulse radiating antenna," in *Sensor and Simulation Notes #479* (C. E. Baum, ed.), Albuquerque, NM: Air Force Research Laboratory, 2003.

[16] M. J. Baretela and J. S. Tyo, "Selective trimming of impulse radiating apertures to increase prompt radiated fields," in *Sensor and Simulation Notes #461* (C. E. Baum, ed.), Albuquerque, NM: Air Force Research Laboratory, 2001. contact AFRL Public Affairs +1-505-846-1911.

[17] M. J. Baretela and J. S. Tyo, "Improvement of prompt radiated response from impulse radiating antennas by aperture trimming," *IEEE Trans. Antennas Propagat.* To be published, September 2003.

[18] C. E. Baum, "Focused aperture antennas," in *Sensor and Simulation Notes #306* (C. E. Baum, ed.), Albuquerque, NM: Air Force Weapons Laboratory, 1987. contact AFRL Public Affairs +1-505-846-1911.

[19] C. Rappaport, "A colormap for effective black and white rendering of color-scale images," *IEEE Antennas and Propagat. Mag.*, vol. 44, pp. 94 – 96, June 2002.

[20] E. G. Farr and C. E. Baum, "A simple model of small-angle TEM horns," in *Sensor and Simulation Notes #340* (C. E. Baum, ed.), Albuquerque, NM: Phillips Laboratory, 1992. contact AFRL Public Affairs +1-505-846-1911.